Reversible fuel electrode supported solid oxide cells fabricated by aqueous multilayered tape casting

Journal of Physics: Energy

PAPER

Reversible fuel electrode supported solid oxide cells fabricated by aqueous multilayered tape casting

L Bernadet[1], M Morales[2], X G Capdevila[3], F Ramos[3], M C Monterde[4], J A Calero[4], A Morata[1], M Torrell[1] and A Tarancón[1,5]

[1] IREC, Catalonia Institute for Energy Research, Department of Advanced Materials for Energy Applications, Jardins de les Dones de Negre 1, Sant Adrià del Besós, Barcelona 08930, Spain
[2] UPC, Universitat Politècnica de Catalunya, Department of Materials Science and Engineering, Campus Diagonal Besòs-EEBE, Barcelona 08019, Spain
[3] FAE, Francisco Albero SAU, Políg. Ind. Gran Vía Sud, Carrer de Rafael Barradas, 19, L'Hospitalet de Llobregat, Barcelona 08908, Spain
[4] AMES, Carrer de Laureà Miró, 388, Sant Feliu de Llobregat, Barcelona 08980, Spain
[5] ICREA, Passeig Lluís Companys 23, Barcelona 08010, Spain

E-mail: lbernadet@irec.cat

Keywords: power to gas, solid oxide fuel cells, solid oxide electrolyser cells, hydrogen, tape casting, degradation, SOC scale up

Supplementary material for this article is available online

OPEN ACCESS

RECEIVED
7 August 2020

REVISED
5 November 2020

ACCEPTED FOR PUBLICATION
10 December 2020

PUBLISHED
28 January 2021

Abstract

Fuel electrode supported solid oxide cells (SOCs) have been developed on an industrial scale using the aqueous tape-casting technique. The NiO–yttria-stabilized zirconia Y_2O_3–ZrO_2 (YSZ) fuel electrode and YSZ electrolyte have been manufactured by multilayer co-laminated tape casting. Details of the tape-casting slurry formulations are described and discussed. Two types of cells were fabricated with different microstructures of the NiO–YSZ support discussed. Good electrochemical performance and stability in SOFC mode at 750 °C and 0.7 V for both button cells reaching around >0.75 W cm^{-2} and with no measurable degradation after >700 h were observed. The selected cell was scaled up to large-area cells (36 cm^2 of the active area) and electrochemically tested at 750 °C in a single repetition unit (SRU) in SOFC (Solid Oxide Fuel Cell), SOEC (Solid Oxide Electrolysis Cell) and co-SOEC (Solid Oxide co-Electrolysis Cell) mode, and in a short-stack of two SRUs in SOFC mode. A current up to 17 A was obtained at 1.4 V (0.7 V $cell^{-1}$) with the short-stack configuration in SOFC mode, corresponding to ∼0.5 A cm^{-2} and 24 W. The performances of the aqueous-based SOC cells can be considered highly remarkable, thus supporting the success in scaling the fabrication of SOC stacks using more environmentally friendly processes than conventional ones.

1. Introduction

Global warming and air pollution represent a big concern for society and affect the policies and regulations of mobility and energy-intensive industries. To reach CO_2 emission neutrality by 2050, several decarbonization strategies are being explored mainly based on renewable energy sources [1]. However, the main problems associated with a renewable energy scenario are the matching of supply and energy demand and all the industrial and transport demands that cannot be straightforwardly electrified. In this scenario, hydrogen arises as one of the most promising solutions to be used as a sustainable energy vector within schemes able to convert renewable electricity into a gas easy to transport and store. Power-to-gas and gas-to-power routes (P2G and G2P) are considered the key to deploying variable renewable energy sources beyond their direct application as an electricity source. Moreover, those P2G and G2P routes are smartly coupling the two major energy infrastructures of our modern society, i.e. gas and electricity networks [2].

Solid oxide cell (SOC) technology is an efficient electrochemical converter to either store electricity from renewable sources, in the form of hydrogen or syngas, or produce electricity and heat from clean hydrogen. The highly efficient reversibility and low electrical consumption, which are related to the high operating

temperatures (650 °C–900 °C), make SOC technology a preferred mid-term option against other types of fuel cells and electrolysers like proton exchange membrane cells (PEM) and alkaline cells (AC) [3]. However, PEM and AC are more mature technologies due to their lower operating temperatures (20 °C–200 °C), which simplifies the material requirements and balance of plant [4].

SOC technology is based on different ceramic materials assembled in multi layers that needs to be robust, efficient, durable and affordable. State-of-the-Art (SoA) cells are composed of an electrolyte based on yttria-stabilized zirconia Y_2O_3–ZrO_2 (YSZ), a fuel electrode made of NiYSZ cermet and an oxygen electrode formed by a composite of $La_{1-x}Sr_xMnO_{3-\delta}$ and YSZ (LSM–YSZ) or by mixed ionic–electronic conductors such as $La_{1-x}Sr_xCo_{1y}Fe_yO_{3-\delta}$ (LSCF). In contrast to LSM–YSZ, LSCF does not present problems like delamination and large polarization losses at intermediate temperatures (IT) [5, 6], which has converted it into the SoA oxygen electrode for IT–SOCs. However, LSCF reacts with the typical YSZ electrolyte forming $SrZrO_3$ insulating phases, which requires the use of a diffusion barrier of $Ce_{1-x}Gd_xO_{2-\delta}$ (GDC) that prevents dramatic polarization losses [7]. Regarding the configuration, depending on the supporting layer, one can define fuel electrode supported cells (FESC) or electrolyte supported cells (ESC) [8]. FESC and ESC configurations should present a functional and mechanical balance between thickness and supporting-layer porosity to allow a good gas circulation between the electrode surface and the reactive sites, in the first case, and between thickness of the electrolyte and its ohmic resistance to minimize the total area specific resistance of the device (ASR), in the second case [9].

Tape-casting and screen-printing techniques are typically used for mass manufacturing of both FESC and ESC SOCs [10–12]. More specifically, tape casting is devoted to the manufacture of supporting layers with a thickness from few to several hundred microns, while screen-printing is used for deposition of thinner layers on top. Green tape quality depends on various parameters, like the slurry solvent, binder, surfactant, dispersant and plasticizer, while the final microstructure of the sintered layer is controlled by the type of pore former, the solvent and the sintering process [13–15]. Tape-casting solvent can be either organic or aqueous. Organic solvents present the advantage of easier slurry preparation due to similar dielectric constants as the ceramic powders [16, 17]. However, organic-based tape casting is not environmentally friendly due to the use of toxic solvent and hazardous additives. Those elements are also problematic from a health and safety point of view regarding the risks of flammability, explosion and worker contamination. Fortunately, those risks can be minimized by using water-based slurries, which makes the aqueous-based tape casting attractive for the SOC industry. Nevertheless, slurry formulation is more complex due to the polarity of the water molecule that affects the slurry dispersion and stability [18]. Most of the literature is dedicated to organic-based tape casting applied to SOCs, while only a few publications directly refer to aqueous-based slurries especially formulated for the fabrication of large-area cells. Beyond well-known water-based alumina slurries, dense YSZ and porous NiO–YSZ, YSZ, Sc_2O_3-doped ZrO_2 (SSZ) and LSM films based on aqueous solutions were successfully obtained [19–23]. Regarding porous layers, Cassidy *et al* showed that combining rice starch and PMMA as pore formers allows the formation of different types of porous layers in terms of size and morphology [14]. Zhou *et al* used other types of starch combined with aqueous solutions as a pore former for FESC button cells that provided a power density close to 500 mW cm^{-2} at 0.7 V and 800 °C [24]. Other groups reported large-area YSZ ESCs of 100 cm^2 giving 200 mW cm^{-2} at 0.7 V and 800 °C [25], while large-area FESCs made by multi layer tape casting reached 0.7 W cm^{-2} in a stack configuration with 1 A cm^{-2} at 750 °C [26]. Overall, further work in organic solvent-free formulations for SOC materials is needed to continue the progression in the implementation of environmentally friendly aqueous-based SOC large-scale manufacturing strategies.

In this work, fuel electrode supported SOCs made using aqueous-based tape-casting and screen-printing techniques were fabricated and structurally and electrochemically characterized in fuel cell (SOFC) and electrolysis (SOEC) modes. Advanced microstructural and electrochemical characterization in button cells as well as long-term operation were first conducted to optimize the formulations for a proper cell microstructure. Afterward, large-area cells of 36 cm^2 of active area were produced and tested in single repeating unit (SRU) and short-stack configurations in SOFC, SOEC (steam electrolysis) and co-SOEC (steam and CO_2 co-electrolysis) modes, offering remarkable performance results.

2. Experimental

2.1. Cell fabrication

Two types of button cells were manufactured by Francisco Albero FAE S.A.U [27], based on an aqueous multi layered tape casting process, for the fuel electrode (support and functional layer) and electrolyte, followed by screen-printing for the deposition of the barrier layer and the oxygen electrode. Tape-casting slurries were prepared with a powder:solvent:binder:plasticizer:dispersant mass ratio of 23:5:4:1:1. PEG 400 (Panreac), Duramax B1000 (Rohm and Hass) and Dolapix PC 75 (Zschimmer and Schwarz) were used as the plasticizer, binder and dispersant, respectively, and water was used as a solvent.

Regarding the first type of cell, Cell 1, the support layer of the fuel electrode was made by ball milling powders of NiO (Kceracell), YSZ (8% Y_2O_3–ZrO_2, KCeracell) and rice starch (Sigma–Aldrich) as the pore former with a weight ratio 7:4:1 of NiO:YSZ:starch before being mixed with the previously described slurry for the final tape-cast. The functional layer slurry was prepared following the same approach, using NiO:YSZ in a 3:2 weight ratio, while only YSZ powder was used for the electrolyte slurry. The half-cells were co-sintered at 1350 °C, presenting an area of 8.0 × 8.0 cm^2 and a total thickness around 280 μm, considering a YSZ electrolyte of 12–20 μm YSZ. The second type of cell, Cell 2, was made by adjusting some parameters within the fuel electrode (support and functional layer) composition and thickness. The support was modified by replacing the starch pore former with PMMA (Sigma–Aldrich, Germany) and by sensibly changing the NiO:YSZ:pore former ratio to 4:4:1. The functional layer was also adjusted using a NiO:YSZ mass ratio of 1:1. After assembling the 10 μm electrolyte layer with the fuel electrode layers, green tapes were laser cut to obtain button cells of 2 cm^2 in diameter and 1.54 cm^2 of active area. Finally, a pre-sintering step was performed at 500 °C for 1 h to remove the pore former followed by a sintering step at 1350 °C for 3 h, thereby obtaining a co-sintered half cell with a total thickness of 430 μm.

The previously described procedure for the second type of cells was replicated to fabricate the support and electrolyte of the large-area cells. However, sensible adjustments regarding the support layer porosity and thickness were realized to improve the mechanical strength of the cell, as it is more critical for larger areas. Sintered samples present a size of 7.8 × 7.8 cm^2 and an active area of 36 cm^2 after the barrier layer and oxygen electrode deposition.

A cation diffusion $Gd_{0.2}Ce_{0.8}O_2$ (GDC) barrier layer was screen-printed and sintered at 1250 °C for all the tested cells, to avoid reactivity and generation of insulator secondary phases such as $SrZrO_3$ between the electrolyte and the oxygen electrode, as has been extensively discussed by the community [7, 28–31]. Finally, the oxygen electrode made by $La_{0.6}Sr_{0.4}Co_{0.2}Fe_{0.8}O_3$ (LSCF) was deposited by screen-printing and sintered at 1200 °C, in all cases. All the samples were microstructurally characterized by scanning electron microscopy (SEM, Zeiss Auriga). Special attention has been paid to the quality of the obtained interfaces.

2.2. Electrochemical characterization

Electrochemical characterization of button cells was carried out in a commercial ProboStatTM (NorECs AS) sample holder placed inside a high-temperature tubular furnace and employing a potentiostat/galvanostat PARSTAT 2273. Gas tightness between the fuel and oxygen chambers was ensured using a Ceramabond™ ring covering the sample edge. Pt meshes on both sides of the cell were used as current collectors. Moreover, the current collection was enhanced by using Ni slurries at the fuel electrode and a commercial LSCF paste (KCeracell) at the oxygen electrode.

Large-area cells were tested in a homemade test bench able to measure either single cells or stacks. The test bench was equipped with a DC power supply and electronic loads that allowed reversible operation. An SRU consisting of a large-area cell and two interconnectors, was initially assembled as follows, before being placed on the system. Compressive sealing, Ni foam at the fuel electrode and Ag mesh at the oxygen electrode were used to avoid gas leakage and to ensure the current collection, respectively. Moreover, current collection was enhanced by painting the fuel electrode and oxygen electrode with Ni paste and LSC ink, respectively. Interconnectors developed and manufactured by AMES [32] were placed between the cell and the system endplates to ensure a proper gas distribution. Once the SRU set inside the test bench, 40 kg were loaded on top of it through a four-point spring compressive system.

Independently of the cell size, heating and cooling ramps of 1 °C min^{-1} were employed. After the sealing and fuel electrode reduction processes, the cell temperature was maintained at 750 °C for the whole set of electrochemical characterizations. For the purposes of clarity, details about the fuel composition or fuel and air flows are specified in the title of each figure. SOFC and SOEC operation modes were characterized by means of polarization curves. Moreover, long-term operations and reversibility cycling (SOFC and SOEC) were carried out for the complete characterization of the produced cells. Electrochemical impedance spectroscopy (EIS) was also performed on button cells in a range of frequencies from 1 MHz to 0.1 Hz and by applying an AC signal of 50 mV–100 mV, under open circuit voltage (OCV) conditions, 0.7 V (SOFC) and 1.3 V (SOEC), to obtain more information about the electrochemical behaviour of the cells under the different operation modes and to evaluate their reversibility.

3. Results and discussion

3.1. Characterization of button cells

3.1.1. Microstructural properties

Figure 1 shows the initial microstructures for two types of cell supports fabricated during the present study. SEM images for each cell support at low and high magnifications are presented in figures 1(a)–(d). Two

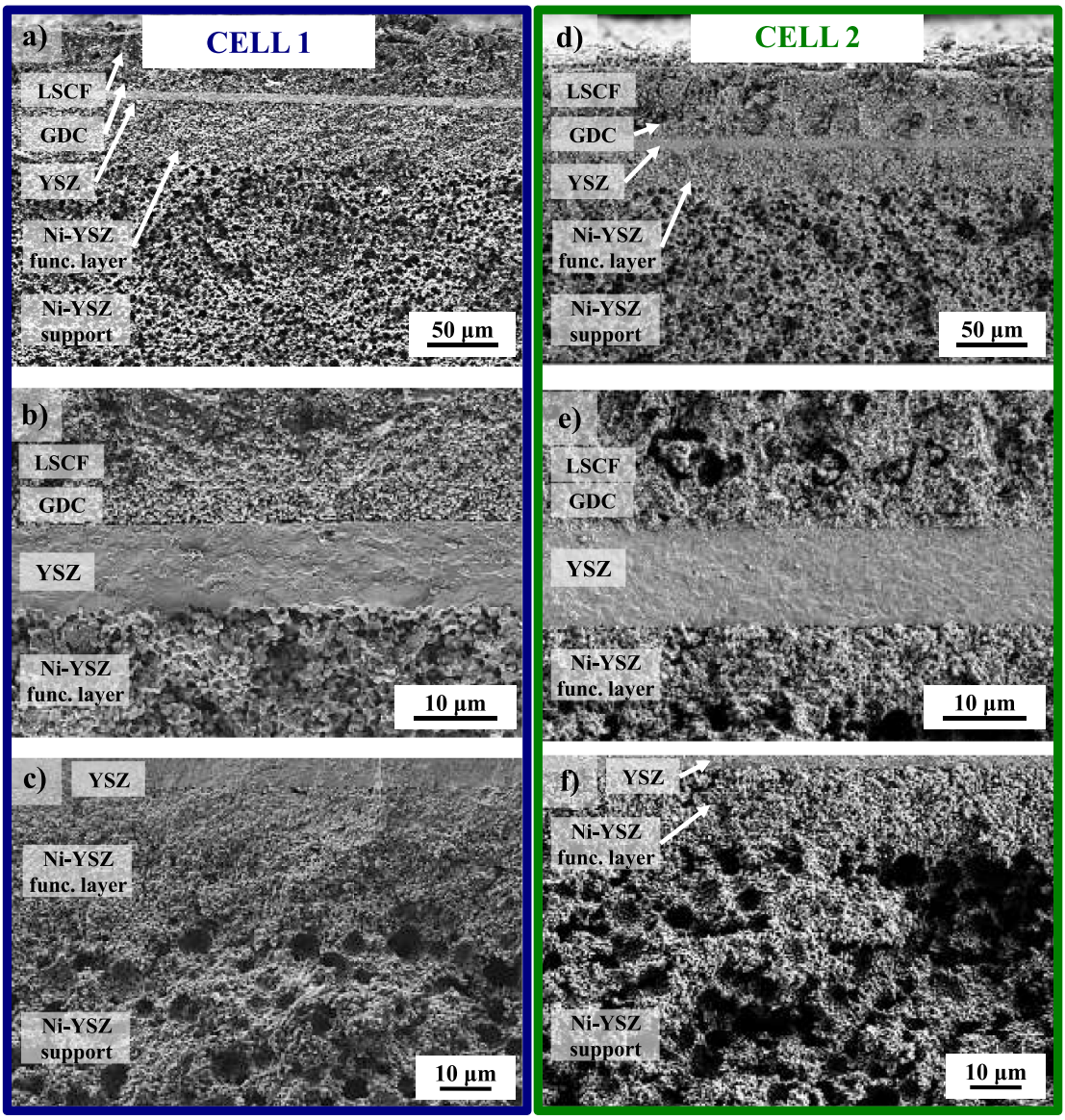

Figure 1. SEM images of the fuel electrode supported Cells 1 and 2: (a) and (b) a general view of the cross section, (c) and (d) the fuel functional layer/electrolyte/barrier-layer/oxygen electrode, and (e) and (f) the fuel functional and support layers.

different tape-cast support microstructures were obtained using two different pore formers. The support of Cell 1 fabricated with 28% starch (v/v), as a pore former, presented a porosity of ∼16% (before reduction). The thickness of this support was of ∼200 μm to achieve enough percolation of gas fuel and the mechanical requirements of a cell support. In contrast, the support of Cell 2 with 28% PMMA exhibited 26% porosity, which may significantly ease the fuel diffusion, while decreasing the flexural strength. To guarantee the required mechanical properties, the support thickness was increased to ∼400 μm. Similar microstructures can be appreciated for the regions of fuel function layer/electrolyte/barrier-layer/electrolyte/oxygen electrode (figures 1(e) and (f)). Note that the 15 μm thick YSZ electrolyte presents a high density that guarantees the desired gas tightness and low ohmic resistance contribution. Additionally, a homogeneous 2 μm thick CGO barrier layer was deposited to avoid the reactivity between the LSCF oxygen electrode and YSZ electrolyte during the LSCF sintering. A good interfacial adhesion between the electrolyte and both electrodes are also evidenced, which is a crucial aspect for good cell performance and stability in the long-term. Finally, both the fuel functional layer and the oxygen electrode present small pore and particle sizes, thus achieving high active surface areas.

3.1.2. Electrochemical tests under SOFC mode

After microstructural analyses, button cells with different types of support were electrochemically characterized. In the first electrochemical test, the *j*–*V* polarization curves under SOFC mode for both cells

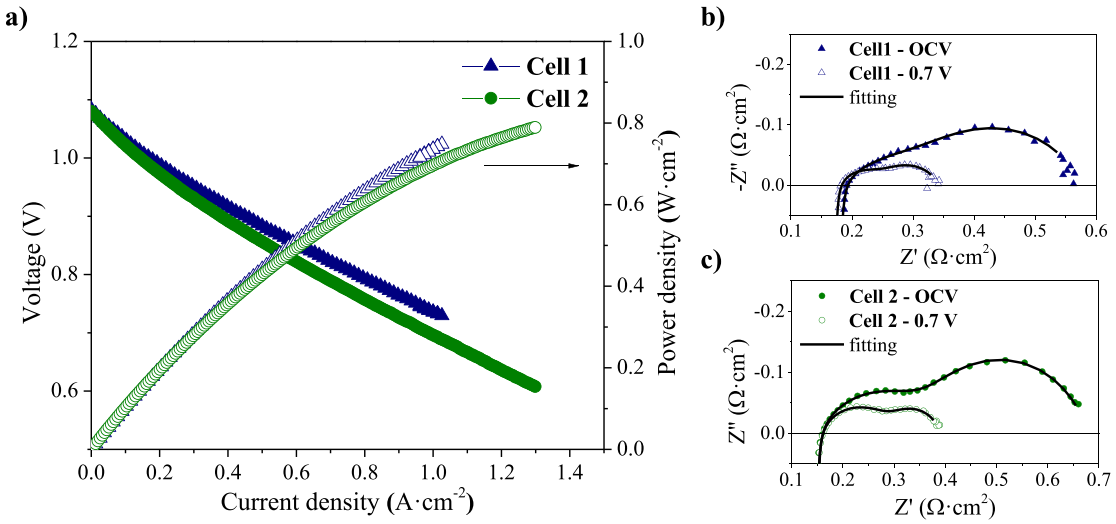

Figure 2. (a) The *j–V* and *j–P* curves for Cells 1 and 2, and Nyquist plots of the EIS spectra measured at 750 °C (b) for Cell 1 and (c) for Cell 2 in SOFC mode under 40 ml min^{-1} cm^{-2} of humidified H_2 at the fuel electrode and 100 ml min^{-1} cm^{-2} synthetic air at the oxygen electrode.

were determined (figure 2(a)). The performance of Cell 1 was slightly better than Cell 2, reaching power densities around 0.80 W cm^{-2} (by extrapolation) and 0.75 W cm^{-2} for Cells 1 and 2, respectively, at the operation point of 0.7 V under wet H_2 and 750 °C. Figures 2(b) and (c) exhibit the EIS results for both cells obtained at OCV and at an operation point of 0.7 V. The impedance spectra were perfectly fitted to an equivalent circuit based on an inductance element (L) connected in series with a serial resistance (R_s) and two ZARC elements composed of a resistance and constant phase elements. The total resistance is slightly lower for Cell 1 (0.57 Ω cm^2 at OCV and 0.35 Ω cm^2 at 0.7 V) than Cell 2 (0.68 Ω cm^2 at OCV and 0.40 Ω cm^2 at 0.7 V), which is in agreement with the results observed on the *j–V* curves. Whereas at OCV the difference comes from the low frequency arc (10° Hz), it comes mainly from the first arc at the middle frequency (10^2 Hz) at 0.7 V that has a resistance of 0.09 Ω cm^2 for Cell 1 and 0.15 Ω cm^2 for Cell 2. The small difference observed is then probably due to the difference in the functional layer between the cells, while the microstructural change between the supports has no clear impact.

3.1.3. Long-term operation test under SOFC mode

After the SOFC electrochemical characterization, the cells were tested for long-term stability, also under SOFC operation conditions at 750 °C, in potentiostatic mode at a voltage of 0.72 V for Cell 1 and in galvanostatic mode at a current density of 0.65 A cm^{-2} for Cell 2 (figures 3(a) and (b)), which corresponds to a power density of 0.45 W cm^{-2} in both cases. For both cells, two differentiated regions may be observed. In the first region, an initial performance drop is evidenced during the first ∼300 h and ∼60 h for Cells 1 and 2, respectively. It is attributed to the typical electrode conditioning commonly associated with the microstructure conditioning of the ionic and electronic percolation paths and the porosity distribution of the required morphology for the imposed operation conditions. After the first region, both cells maintained an almost constant performance with small oscillations for >3000 h for Cell 1 (see figure 1 of the supplementary information (available online at stacks.iop.org/JPENERGY/3/024002/mmedia)) and 600 h for Cell 2. In these ranges of time, the degradation rates are slightly negative, around −0.02% kh^{-1} and −1% kh^{-1} for Cells 1 and 2, respectively and, therefore, may be considered negligible. In figure 3, the results of the EIS tests confirmed a moderate increase in the ohmic and polarization resistances for both cells in OCV and operating at 0.7 V. In Cell 1, for the 0–700 h period, the ohmic resistances were increased around 0.07 Ω cm^{-2} (at OCV and 0.7 V), and the polarization resistances augmented 0.23 Ω cm^{-2} and 0.21 Ω cm^{-2} at OCV and 0.7 V, respectively. In Cell 2, the ohmic resistance was almost constant between 0 h and 700 h, and the polarization resistances increased 0.02 Ω cm^{-2} and 0.07 Ω cm^{-2} at OCV and 0.7 V, respectively. For both cells, the increase in polarization resistance comes from the middle frequency arc that is usually attributed to the charge transport phenomena at the electrode [33]. Considering the low degradation rates, this increase for both cells can be attributed to the electrode microstructure conditioning, which was more significant for Cell 1, as observed in figures 3(a) and (c). Therefore, both cells with different support designs presented a good performance and long-term stability in SOFC mode.

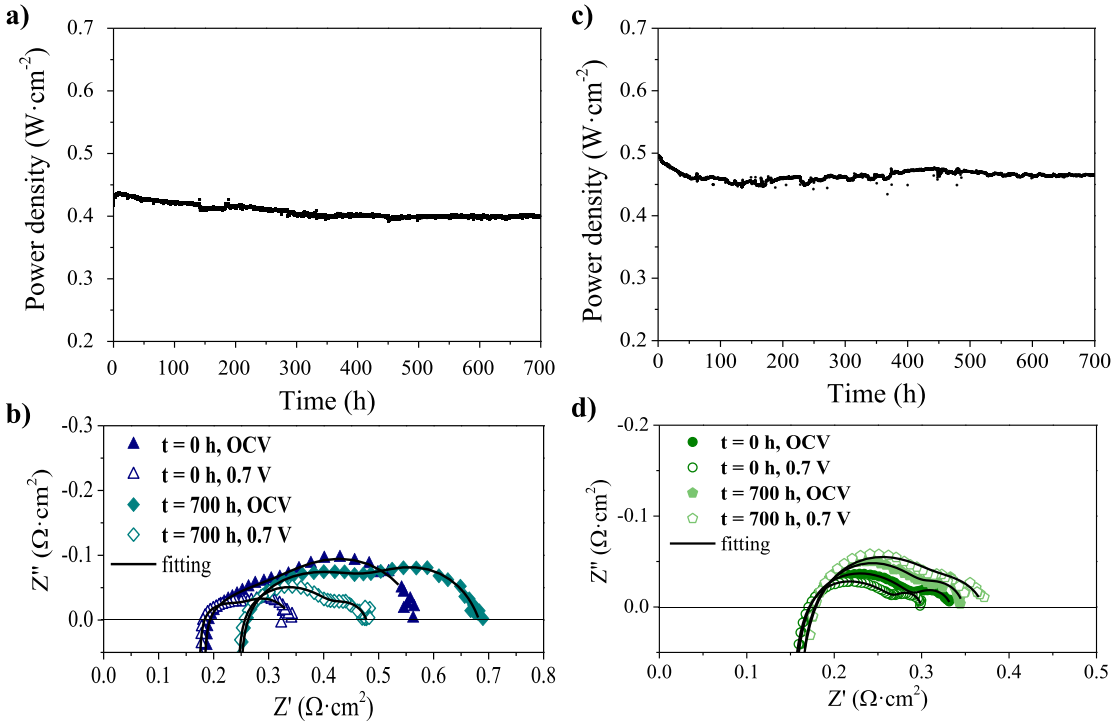

Figure 3. Evolution of the power densities and the corresponding Nyquist plots of the EIS spectra, during aging tests determined at 750 °C, in SOFC mode, under pure H_2 at the fuel electrode and synthetic air at the oxygen electrode, for: (a) and (b) Cell 1 at 0.72 V, and (c) and (d) Cell 2 at 0.66 A cm^{-2}.

3.1.4. Reversibility test under SOFC/SOEC modes

Once the performance of the developed cells on SOFC was fully characterized, their potential reversibility was studied using an SOFC/SOEC cycling test using a feeding gas composition of 33% of H_2O and 67% H_2. The *j–V* curves of cells from SOFC mode to SOEC mode are presented in figure 4. Although the performance in SOFC mode is similar for both series (ASR = 0.25 Ω cm^{-2}), one can see that Cell 1 exhibits a strong increase in the *j–V* curve slope at high electrolysis current densities above −0.4 A cm^{-2}, whereas Cell 2 presents a smaller *j–V* slope change at current densities higher than −0.6 A cm^{-2}. At the operation point of 1.3 V, Cells 1 and 2 present high ASR values of 1.25 Ω cm^{-2} and 0.77 Ω cm^{-2}, respectively. These signs of cell starvation, especially shown by Cell 1, are typically ascribed to microstructural problems of the support, related to a lack of porosity that hinders the fuel/water diffusion through the fuel electrode support microstructure [34]. These results are in clear agreement with the already commented on lower porosity presented by the microstructure of the fuel electrode of Cell 1. It means that operating under the thermoneutral voltage for steam electrolysis (1.29 V at 750 °C), while Cell 1 is limited at a maximum current density of <−0.6 A cm^{-2}, Cell 2 may reach around −0.8 A cm^{-2}.

3.1.5. Reversibility cycling SOFC/SOEC tests

From the electrochemical tests under SOFC/SOEC modes, Cell 2 presents the most suitable support microstructure to operate under SOEC mode. Therefore, it was also tested on a more aggressive stability reversible test operation under SOEC/SOFC cycles for almost 700 h (figure 5(a)). The evolution of the voltage for Cell 2 reveals a clear difference in degradation rate depending on the operation mode. In each reversible cycle, the cell voltage under SOEC mode is slightly increased, whereas it remained almost stable under SOFC mode. After accumulating 19 reversible cycles, considering the first one as electrode microstructure conditioning, the degradation rates are around ∼3.5% kh^{-1} in SOEC mode and <1.0%/k h^{-1} in SOFC mode. The same tendency is observed from the EIS tests (figure 5(b)). The comparison of the EIS curves at 0 h and after 700 h (after 20 reversible cycles) evidences the small variation of the total resistance under 0.7 V (SOFC mode) versus a significant increase at 1.3 V (SOEC mode). Regarding the ohmic resistance, it is nearly identical at 0 h and 700 h in both cases. However, as observed in the previous long-term test, the polarization resistance is the one increasing after 700 h. There is a clear increase of both arcs at OCV (10^2 and 10° Hz), while in SOFC mode at 0.7 V, only the first arc (10^2 Hz) is slightly increasing compared to the impedance at initial time. In SOEC mode at 1.3 V, a strong increase of both arcs is observed compared to EIS data at 0 h but also at OCV after 700 h. The change in the low

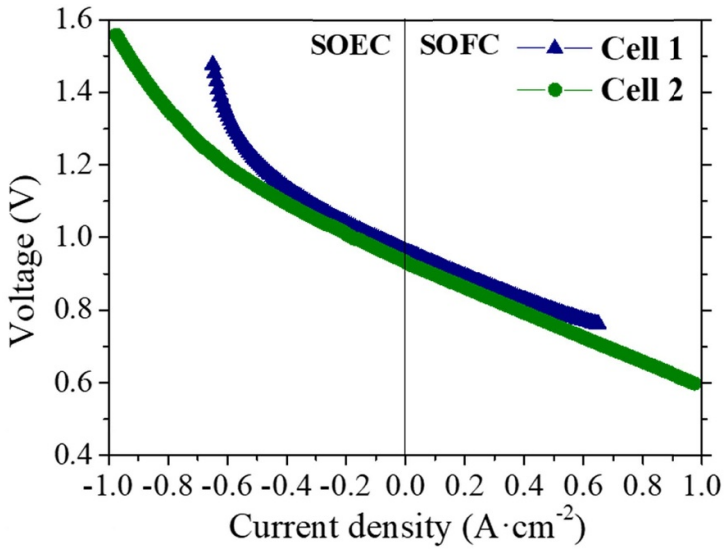

Figure 4. The *j*–*V* curve of Cell 2, determined at 750 °C in SOFC and SOEC modes under 40 ml min^{-1} cm^{-2} fuel with a 33/67 H_2O/H_2 ratio to the fuel electrode and 100 ml min^{-1} cm^{-2} synthetic air at the oxygen electrode.

frequency arc (10° Hz) can be attributed to an increase in the diffusion and conversion issues related to the gas and water transport inside the electrodes, whereas the middle frequency increase can come from a degradation of the pathway for the charges inside the electrodes [35]. It is worth mentioning that the difference in degradation behaviour between SOFC and SOEC modes has been studied in recent years and can be ascribed to a higher depletion of Ni inside the functional layer of the fuel electrode in SOEC mode [36–39]. Degradation issues at the oxygen electrode with Sr diffusion and $SrZrO_3$ formation at the interface YSZ/CGO/LSCF were also found to be more important in SOEC operation than SOFC [40].

3.1.6. Post-test microstructural analysis

The cells tested in the present study were observed by SEM with the aim of identifying the degradation mechanisms under different operational conditions. The post-test analysis of electrolyte and electrodes are discussed here and are related to the electrochemical issues observed during the long-term tests. Figure 6 shows the most significant details of the electrolyte–electrode cross-section region for the cells after aging under SOFC and reversible SOEC/SOFC cycling tests. The electrolyte microstructure of aged SOFC cells presents the typical intragranular fracture surface (figures 6(a) and (b)), which is identical to a fresh cell (figures 1(c)–(f)) [41, 42]. In contrast, the electrolyte of the SOEC/SOFC cycled cell evidences an intergranular fracture mode (figure 6(c)) [43]. Probably, it is related to the high concentration of pores and voids observed near the fuel electrode/electrolyte interface. These voids present an elongated form, probably due to the combination and propagation of small voids through the grain boundaries, along the electrolyte, progressing from the oxygen electrode side to the hydrogen electrode one. Thus, the combination of voids generates irregular defects at the electrolyte that may reduce the mechanical strength and the contact area between the electrolyte and electrodes. A similar degradation was also reported elsewhere [43–45], when cells with the same architecture were operated in SOEC mode at relatively high current densities. The origin of pores and voids at the electrolytes of cells operated under SOEC/SOFC cycles is probably due to the cation diffusion in the electrolyte, which is produced by the higher oxygen pressure in SOEC mode compared to SOFC mode. Considering the different degradation rate between SOEC and SOFC, the electrolyte degradation and the possible delamination at the LSCF/CGO interface, which is not clearly observed by SEM, may contribute to the voltage increase under SOEC, during the SOEC/SOFC cycling test.

3.2. Characterization of large-area cells

3.2.1. Microstructural and morphological analysis

From the electrochemical analyses of button cells, Cell 2 evidenced the best balance between the electrochemical and mechanical properties to operate under reversible SOEC/SOFC cycling tests. Therefore, button Cell 2 was scaled up to large-area cells with an active area of 36 cm^2 (figure 7(a)).

Figure 8 shows representative cross-section SEM images of the electrolyte–electrode interfaces for both oxygen and fuel sides in large-area cells. Good homogeneity in thickness, especially in the critical electrolyte, are observed. Full dense electrolytes, with the presence of low levels of closed porosity, and homogeneously

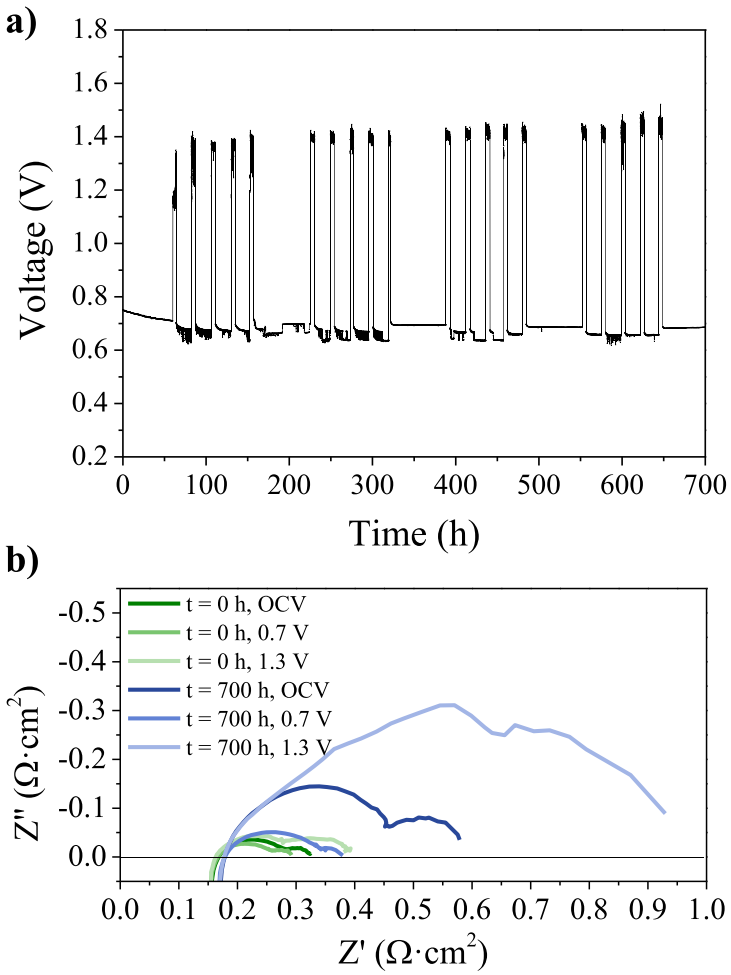

Figure 5. (a) Evolution of voltage in a reversible cycling test, (b) Nyquist plots of the EIS spectra, for Cell 1, at 750 °C, in SOFC mode at 0.66 A cm^{-2} and SOEC mode at −0.66 A cm^{-2} (40 ml min^{-1} cm^{-2} of fuel with a 33/67 H_2O/H_2 ratio and 100 ml min^{-1} cm^{-2} synthetic air at the oxygen electrode). The atmosphere at the fuel electrode is switched to pure H_2 between five cycles, for 72 h, before starting a new series.

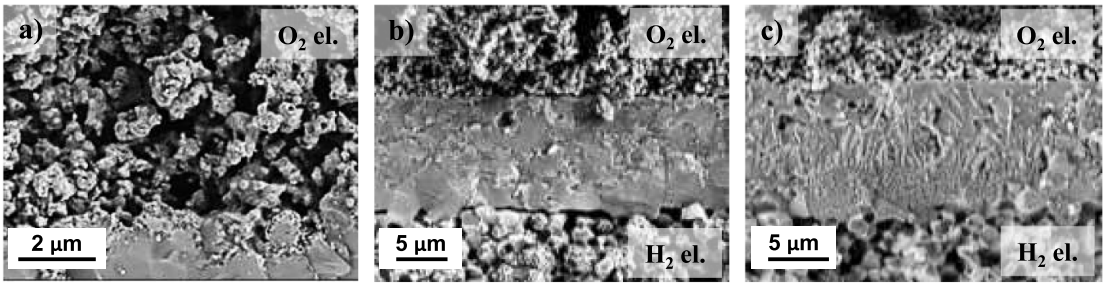

Figure 6. SEM images of the fuel functional layer/electrolyte/barrier-layer/oxygen electrode region for: (a) Cell 1, after 3500 h, operating under SOFC mode, (b) Cell 2 after aging for 700 h (c) Cell 2, after 700 h operating under a reversible SOEC/SOFC cycling test.

porous electrodes were also obtained (figure 8(a)). Finally, figure 8(b) shows a detail of the great adhesion observed between all the layers in the core of the cell, which is especially critical on the oxygen side for the combination of layers consisting of fuel functional/electrolyte/barrier layer/oxygen electrode (figure 8(c)).

3.2.2. Electrochemical tests

Large-area cells of type 2 were fabricated by FAE at an industrial scale with a shape compatible with current collectors and end plates developed by AMES (figure 7(a)). These cells were assembled in SRUs consisting of two interconnects and one cell and short-stacks consisting of two SRUs (figures 7(b) and (c)). Compressive sealings were employed to facilitate the assembly.

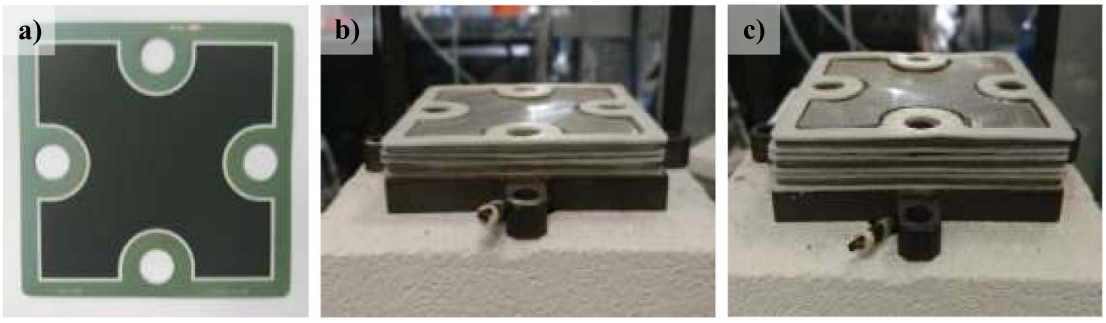

Figure 7. Pictures of (a) the large-area cell, (b) the SRU and (c) the short-stack made with two large-area cells placed on top of the lower endplate inside the test station.

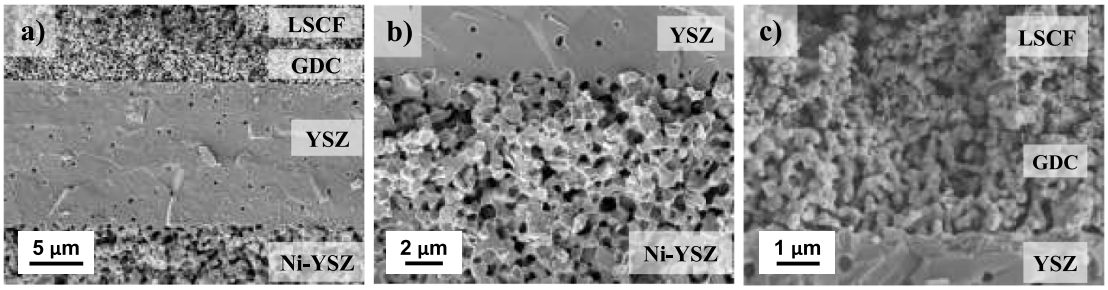

Figure 8. SEM images of the large-area cell: (a) a general view of the electrolyte in cross section, (b) the fuel functional/electrolyte interlayer, and (c) the interlayer between the electrolyte, the barrier layer and the oxygen electrode.

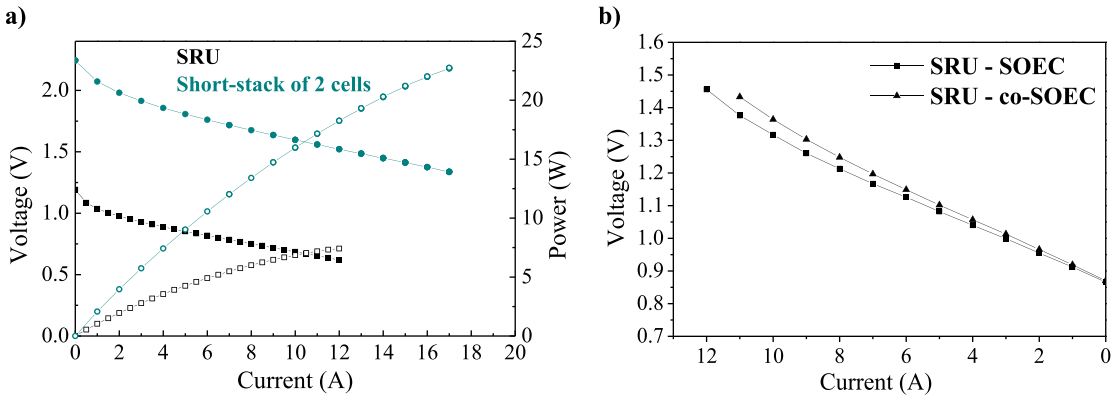

Figure 9. (a) *I–V* and *I–P* curves for both the SRU and short-stack of two large-area cells in SOFC mode at 750 °C (25 Nml min^{-1} cm^{-2} of H_2 at the fuel electrode and 80 Nml min^{-1} cm^{-2} of synthetic air at the oxygen electrode), and (b) the *I–V* curve for the SRU in SOEC and co-SOEC mode at 750 °C (50 Nml min^{-1} cm^{-2} of 90/10 H_2O/H_2 or 65/25/10 $H_2O/CO_2/H_2$ at the fuel electrode and 150 Nml min^{-1} cm^{-2} of synthetic air at the oxygen electrode).

Figure 9(a) shows the *I–V* polarization curves for the SRU and stack, under SOFC mode, in operational conditions comparable to the previously described button cells, i.e. under pure wet H_2 at 750 °C. The SRU and the two-unit short-stack present the expected OCV (1.19 and 2.24 V, respectively), indicating a gastight sealing in both cases. While the SRU shows a maximum power of ∼8 W, the short-stack approaches 24 W, which is not corresponding to the expected two-fold increase. This suggests an important contribution of the common elements, e.g. endplates and current collectors, to the total resistance of the SRUs and stacks in our setup. Taking this into account (and the results obtained for button cells), excellent values of resistance are obtained for the large-area cells and interconnects, which share, almost equally, the ASR of the whole stack. Correspondingly, figure 9(b) shows the *I–V* curves for the SRU, under SOEC and co-SOEC modes, at 750 °C, and 90/10 H_2O/H_2 and 65/25/10 $H_2O/CO_2/H_2$, respectively. In both electrolysis modes, it was possible to inject in the SRU currents as high as 10 A at 1.3 V. Although the *I–V* curves for both electrolysis modes are quite similar, the cell performance under SOEC mode presents slightly better behaviour than under co-SOEC

operational conditions. This is attributed to the low activation/conversion efficiency of CO_2, which may also affect the degradation issues in the long-term, as reported in previous studies [46]. More extensive research studies of the cell degradation in the long-term under SOFC and SOEC modes will be carried out in further works to determine the stability of the aqueous-based large-area SOC cells fabricated here.

4. Conclusions

Multilayer aqueous tape casting of co-laminated and co-sintered half-cells consisting of a NiO–YSZ support, an YSZ electrolyte and a fuel functional electrode have been developed at an industrial scale and obtained remarkable electrochemical performance.

Preliminary electrochemical tests based on button cells evidenced for both cells a good performance and great long-term stability in SOFC mode, as no measurable degradation was observed after >3000 h and 600 h (after a first stabilization step) for Cell 1 and Cell 2, respectively.

Cell 2 was scaled up to large areas (36 cm^2 of active surface) and electrochemically tested at 750 °C in an SRU, consisting of two interconnects and one cell, and also in a short-stack, consisting of two SRUs. The SRU was able to deliver a maximum power of ∼8 W in SOFC mode and accept a total of 10 A of current at 1.3 V in SOEC and co-SOEC operating conditions. Interestingly, the two-unit short-stack was able to produce ∼24 W under the very same SOFC conditions as the SRU, indicating the presence of excessively resistive common elements in the setup. Taking this into account, the performance of the aqueous-based SOC cells can be considered highly remarkable, thus supporting the success in scaling the fabrication of SOC stacks using more environmentally friendly processes than conventional ones.

Acknowledgments

The authors want to acknowledge the financial support of the 'Generalitat de Catalunya' (2017 SGR 1421, NANOEN) and the 'Institut de Cultura de Barcelona' for the financial support of the project HY-BCN (19S01452-006).

ORCID iDs

M Morales https://orcid.org/0000-0003-0702-1966
M Torrell https://orcid.org/0000-0002-3946-1352
A Tarancón https://orcid.org/0000-0002-1933-2406

References

[1] Parra D, Valverde L, Pino F J and Patel M K 2019 A review on the role, cost and value of hydrogen energy systems for deep decarbonisation *Renew. Sustain. Energy Rev.* **101** 279–94
[2] Ebbesen S D, Jensen S H, Hauch A and Mogensen M B 2014 High temperature electrolysis in alkaline cells, solid proton conducting cells, and solid oxide cells *Chem. Rev.* **114** 10697–734
[3] Fu Q, Mabilat C, Zahid M, Brisse A and Gautier L 2010 Syngas production via high-temperature steam/CO_2 co-electrolysis: an economic assessment *Energy Environ. Sci.* **3** 1382
[4] Ruiz-Morales J C, Marrero-López D, Gálvez-Sánchez M, Canales-Vázquez J, Savaniu C and Savvin S N 2010 Engineering of materials for solid oxide fuel cells and other energy and environmental applications *Energy Environ. Sci.* **3** 1670–81
[5] Chen K, Ai N and Jiang S P 2012 Performance and stability of (La,Sr)MnO_3–Y_2O_3–ZrO_2 composite oxygen electrodes under solid oxide electrolysis cell operation conditions *Int. J. Hydrog. Energy* **37** 10517–25
[6] Keane M, Mahapatra M K, Verma A and Singh P 2012 LSM-YSZ interactions and anode delamination in solid oxide electrolysis cells *Int. J. Hydrog. Energy* **37** 16776–85
[7] Uhlenbruck S, Moskalewicz T, Jordan N, Penkalla H-J and Buchkremer H P 2009 Element interdiffusion at electrolyte-cathode interfaces in ceramic high-temperature fuel cells *Solid State Ion.* **180** 418–23
[8] Mahato N, Banerjee A, Gupta A, Omar S and Balani K 2015 Progress in material selection for solid oxide fuel cell technology: a review *Prog. Mater. Sci.* **72** 141–337
[9] Gómez S Y and Hotza D 2016 Current developments in reversible solid oxide fuel cells *Renew. Sustain. Energy Rev.* **61** 155–74
[10] Battelle Memorial Institute 2014 Manufacturing cost analysis of 1 kW and 5 kW solid oxide fuel cell (SOFC) for auxiliary power applications *Report* (Golden, CO: Battelle Memorial Institute)
[11] Cassidy M 2017 Trends in the processing and manufacture of solid oxide fuel cells *Wiley Interdiscip. Rev. Energy Environ.* **6** e248
[12] Harboe S, Schreiber A, Margaritis N, Blum L, Guillon O and Menzler N H 2020 Manufacturing cost model for planar 5 kWel SOFC stacks at Forschungszentrum Jülich *Int. J. Hydrog. Energy* **45** 8015–30
[13] Chen X *et al* 2019 Electrochemical property of multi-layer anode supported solid oxide fuel cell fabricated through sequential tape-casting and co-firing *J. Mater. Sci. Technol.* **35** 695–701
[14] Cassidy M, Doherty D J, Yue X and Irvine J T S 2015 Development of tailored porous microstructures for infiltrated catalyst electrodes by aqueous tape casting methods *ECS Trans.* **68** 2047–56
[15] Michálek M, Blugan G, Graule T and Kuebler J 2015 Comparison of aqueous and non-aqueous tape casting of fully stabilized ZrO_2 suspensions *Powder Technol.* **274** 276–83

[16] Yuan C, Liu Y, Zhou Y, Zhan Z and Wang S 2013 Fabrication and characterization of a cathode-support solid oxide fuel cell by tape casting and lamination *Int. J. Hydrog. Energy* **38** 16584–9
[17] Liu Z, Liu M, Nie L and Liu M 2013 Fabrication and characterization of functionally-graded LSCF cathodes by tape casting *Int. J. Hydrog. Energy* **38** 1082–7
[18] Baquero T, Escobar J, Frade J and Hotza D 2013 Aqueous tape casting of micro and nano YSZ for SOFC electrolytes *Ceram. Int.* **39** 8279–85
[19] Rahmawati F, Pratiwi A and Lestari W W 2019 Preparation of yttria-stabilized zirconia film from an aqueous nano-grain suspension for solid electrolyte *J. Dispers. Sci. Technol.* **40** 1280–7
[20] Gómez L, Colomer M T, Escobar J and Moreno R 2013 Manufacture of a non-stoichiometric LSM cathode SOFC material by aqueous tape casting *J. Eur. Ceram. Soc.* **33** 1137–43
[21] Goulart C and de Souza D 2017 Critical analysis of aqueous tape casting, sintering, and characterization of planar yttria-stabilized zirconia electrolytes for SOFC *Int. J. Appl. Ceram. Technol.* **14** 413–23
[22] Fernández-González R, Molina T, Savvin S, Moreno R, Makradi A and Núñez P 2014 Fabrication and electrical characterization of several YSZ tapes for SOFC applications *Ceram. Int.* **40** 14253–9
[23] Ramanathan S and Kakade M B 2011 Aqueous slurry processing of monolithic films for SOFC–YSZ, LSM and YSZ–NiO systems *Int. J. Hydrog. Energy* **36** 14956–62
[24] Zhou J, Liu Q, Zhang L, Pan Z and Chan S H 2016 Influence of pore former on electrochemical performance of fuel-electrode supported SOFCs manufactured by aqueous-based tape-casting *Energy* **115** 149–54
[25] Zhou J *et al* 2019 Aqueous tape casting technique for the fabrication of $Sc_{0.1}Ce_{0\cdot01}Zr_{0\cdot89}O_{2+\Delta}$ ceramic for electrolyte-supported solid oxide fuel cell *Int. J. Hydrog. Energy* **44** 21110–4
[26] Morales M *et al* 2018 Enhanced performance of gadolinia-doped ceria diffusion barrier layers fabricated by pulsed laser deposition for large-area solid oxide fuel cells *ACS Appl. Energy Mater.* **1** 1955–64
[27] FAE (Francisco Albero SAU) n.d. Auto-electrical and electronic manufacturarer (available at: www.fae.es/en/)
[28] Wang F *et al* 2014 Sr and Zr diffusion in LSCF/10GDC/8YSZ triplets for solid oxide fuel cells (SOFCs) *J. Power Sources* **258** 281–9
[29] Morales M *et al* 2017 Multi-scale analysis of the diffusion barrier layer of gadolinia-doped ceria in a solid oxide fuel cell operated in a stack for 3000 h *J. Power Sources* **344** 141–51
[30] Matsui T, Li S, Inoue Y, Yoshida N, Muroyama H and Eguchi K 2019 Degradation analysis of solid oxide fuel cells with (La,Sr)(Co,Fe)$O_{3-\delta}$ cathode/Gd_2 O_3–CeO_2 interlayer/Y_2 O_3–ZrO_2 electrolyte system: the influences of microstructural change and solid solution formation *J. Electrochem. Soc.* **166** F295–300
[31] Xu H, Cheng K, Chen M, Zhang L, Brodersen K and Du Y 2019 Interdiffusion between gadolinia doped ceria and yttria stabilized zirconia in solid oxide fuel cells: experimental investigation and kinetic modeling *J. Power Sources* **441** 227152
[32] AMES Group n.d. Manufacturer of sintered parts (available at: www.ames-sintering.com/)
[33] Bertei A, Ruiz-Trejo E, Tariq F, Yufit V, Atkinson A and Brandon N P 2016 Validation of a physically-based solid oxide fuel cell anode model combining 3D tomography and impedance spectroscopy *Int. J. Hydrog. Energy* **41** 22381–93
[34] Njodzefon J-C, Klotz D, Kromp A, Weber A and Ivers-Tiffée E 2013 Electrochemical modeling of the current-voltage characteristics of an SOFC in fuel cell and electrolyzer operation modes *J. Electrochem. Soc.* **160** F313–23
[35] Sun X, Hendriksen P V, Mogensen M B and Chen M 2019 Degradation in solid oxide electrolysis cells during long term testing *Fuel Cells* **19** 740–7
[36] Monaco F *et al* 2019 Degradation of Ni–YSZ electrodes in solid oxide cells: impact of polarization and initial microstructure on the Ni evolution *J. Electrochem. Soc.* **166** F1229–42
[37] Trini M, Hauch A, De Angelis S, Tong X, Hendriksen P V and Chen M 2020 Comparison of microstructural evolution of fuel electrodes in solid oxide fuel cells and electrolysis cells *J. Power Sources* **450** 227599
[38] Hubert M, Laurencin J, Cloetens P, Morel B, Montinaro D and Lefebvre-Joud F 2018 Impact of nickel agglomeration on solid oxide cell operated in fuel cell and electrolysis modes *J. Power Sources* **397** 240–51
[39] Nakajo A *et al* 2020 Evolution of the morphology near triple-phase boundaries in Ni–Yttria stabilized zirconia electrodes upon cathodic polarization *J. Electrochem. Energy Convers. Storage* **17** 1–13
[40] Laurencin J *et al* 2017 Degradation mechanism of $La_{0.6}$ $Sr_{0.4}$ $Co_{0.2}$ $Fe_{0.8}$ $O_{3-\delta}$/$Gd_{0.1}$ $Ce_{0.9}$ $O_{2-\delta}$ composite electrode operated under solid oxide electrolysis and fuel cell conditions *Electrochim. Acta* **241** 459–76
[41] Morales M, Roa J J, Capdevila X G, Segarra M and Piñol S 2010 Mechanical properties at the nanometer scale of GDC and YSZ used as electrolytes for solid oxide fuel cells *Acta Mater.* **58** 2504–9
[42] Roa J J *et al* 2011 Mechanical characterisation at nanometric scale of a new design of SOFCs *Fuel Cells* **11** 124–30
[43] The D *et al* 2015 Microstructural comparison of solid oxide electrolyser cells operated for 6100 h and 9000 h *J. Power Sources* **275** 901–11
[44] Knibbe R, Traulsen M L, Hauch A, Ebbesen S D and Mogensen M 2010 Solid oxide electrolysis cells: degradation at high current densities *J. Electrochem. Soc.* **157** B1209
[45] Rinaldi G *et al* 2017 Post-test analysis on a solid oxide cell stack operated for 10,700 h in steam electrolysis mode *Fuel Cells* **17** 541–9
[46] Zheng Y *et al* 2017 A review of high temperature co-electrolysis of H_2O and CO_2 to produce sustainable fuels using solid oxide electrolysis cells (SOECs): advanced materials and technology *Chem. Soc. Rev.* **46** 1427–63